Journal of Chemical Crystallography (2023) 53:185–196
https://doi.org/10.1007/s10870-022-00959-9

ORIGINAL PAPER

Crystal Structure Characterization, Interaction Energy Analysis and DFT Studies of 3-(4-Chlorophenyl)-*N*-phenylquinoxalin-2-amine

P. Akhileshwari[1] · K. R. Kiran[2] · M. A. Sridhar[1] · M. P. Sadashiva[2]

Received: 9 April 2022 / Accepted: 1 August 2022 / Published online: 16 August 2022

Abstract

The title compound is synthesized, and characterized by spectroscopic and XRD methods. The compound crystallizes in the orthorhombic crystal system with the space group $P2_12_12_1$. The structure exhibits C–H···N intermolecular interaction and π···π interactions. Hirshfeld surface analysis was performed to determine the individual contributions of intermolecular contacts to the crystal packing. The structural and electronic properties of the molecule were investigated by density functional theory method with B3LYP hybrid functional. Intramolecular interactions involved in the crystal structure was analyzed through topological atom-in-molecules analysis and noncovalent interactions method. Molecular electrostatic potential surface shows the chemical reactive regions around the nitrogen and hydrogen atoms.

Graphical Abstract

The article presents the characterization of synthesized compound by single crystal X-ray diffractionmethod. Atom-in-molecules analysis and noncovalent interactions Intramolecularinteractions involved in the crystal structure were analyzed by DFT method.

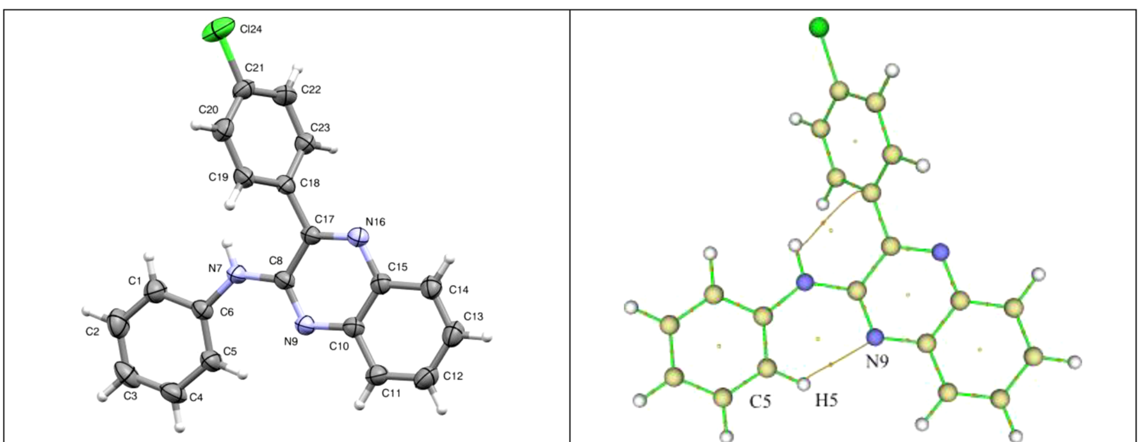

(a) (b)

Keywords Quinoxaline · Crystal structure · DFT · HOMO–LUMO · MEP

✉ M. A. Sridhar
mas@physics.uni-mysore.ac.in

1 Department of Studies in Physics, University of Mysore, Manasagangotri, Mysuru 570 006, India

2 Department of Studies in Chemistry, University of Mysore, Manasagangotri, Mysuru 570 006, India

Introduction

Cancer is one of the serious diseases for the humans, and is the highest leading factor in death worldwide [1, 2]. Compounds having anticancer and antimicrobial activity have to be designed to treat the disease. Some quinoxaline derivatives have a cytotoxic effect on human cancer cell lines [3]. There are many research studies reporting the efficacy of new compounds as potential chemotherapeutic agents. Quinoxaline ring systems constitute the building blocks for natural and synthetic pharmacologically active compounds.

Quinoxaline ring is a part of naturally occurring antibiotics such as echinomycin, triostin A., quinaldopeptin and echinoserinethat [4]. Quinoxaline nucleus is a bioisoster of quinoline, quinazoline, naphthalene and benzothiophene, and represents an important class of heterocyclic compounds [5]. The heterocyclic compounds bearing quinoxaline scaffold are proven to have a good anticancer activity and show promise in the discovery of novel anticancer agents [6]. In addition to the anticancer activity, quinoxaline derivatives display diverse biological activities such as antimicrobial, anticonvulsant, analgesic activities, anti-inflammatory, antiobese, antiviral, and kinase inhibition [7–14]. They are used in industries due to their ability to inhibit the metal corrosions [15]. The organic inhibitors containing heteroatoms such as O, N, and S, are known as good inhibitors for corrosion, as they allow adsorption on the steel surface [16].

Several methods are available for the synthesis of quinoxaline derivatives which involve condensation of 1,2-diamines with α-diketones [17], 1,4-addition of 1,2-diamines to diazenylbutenes [18], cyclizationeoxidation of phenacyl bromides and oxidative coupling of epoxides with ene-1,2-diamines [19]. Different catalysts have been used for the synthesis of quinoxalines, such as $CuSO_4{\cdot}H_2O$, MnO_2, ceric ammonium nitrate, and iodine [20, 21]. Lately cyclocondensation of o-Phenylenediamines with 2-Oxo-ethanimidothioates method has been used to synthesize the novel aryl quinoxalines [22].

These findings have inspired us to synthesize a new set of heterocyclic compounds having quinoxaline moiety. The present article reports the synthesis, spectroscopic characterization and single crystal structure studies of 3-(4-chlorophenyl)-*N*-phenylquinoxalin-2-amine. Density functional theory (DFT) method was used for geometry optimization and frequency calculations. They will provide new insights into electronic, and structure properties.

Materials and methods

All reagents were purchased from commercial suppliers and used without further purification. The reactions were monitored by thin layer chromatography (TLC) using precoated sheets of silica gel (Merck 60F254, 0.25 mm thickness) and visualized under UV light. Melting points were determined with a Selaco melting point apparatus and are uncorrected. ^{1}H and ^{13}C NMR spectra were obtained with a Agilent NMR spectrometer. Chemical shifts (δ) are given in parts per million (ppm) using the residue solvent ($CDCl_3$) peak as reference relative to TMS. Coupling constants (J) are given in Hz. Mass spectral analysis was performed with a Water-Synapt G2 mass spectrometer.

Synthesis of 3-(4-Chlorophenyl)-*N*-phenylquinoxalin-2-amine

Mixture of α-oxodithioester (2.54 mmol) and amine (2.80 mmol) was added to the ice cooled solution of sodium hydride (6.37 mmol) in the solvent dimethylformamide (DMF). The reaction mixture was stirred about 2–3 h. After the completion of reaction, methyl iodide (5.09 mmol) was added, and immediately quenched with cold brine (50 mL) solution. The quenched solution was extracted with ethyl acetate (50 mL × 3) and the combined organic layer was washed with water, dried over sodium sulphate, and concentrated under reduced pressure [22]. The crude mixture was subjected to column chromatography using hexane–ethyl acetate mixture (0.5:9.5::v:v).

A solution of *o*-phenyl diamine and imidothioate in toluene was heated at 80 °C for about 2–4 h. The progress of the reaction was monitored by TLC. After the completion of reaction, the reaction mixture was allowed to attain the room temperature. The product was quenched with ice-cold water (25 mL), extracted with EtOAc (25 mL × 3). The combined organic layer was washed with brine solution (25 mL) and dried over sodium sulphate, and concentrated under reduced pressure. The crude mixture was subjected to column chromatography using hexane–ethyl acetate mixture (1:19::v:v). Column purified sample (yellow solid) was dissolved in hexane by heating. Slow evaporation method was adopted to obtain the crystals (Fig. 1).

Spectroscopic Characterization of 3-(4-Chlorophenyl)-*N*-phenylquinoxalin-2-amine

Yellow solid, yield: 67% [153 mg] M.P. 137-139^{0}C. **IR(KBr):** 3413, 2925, 1527,1491,1443,759,750 cm^{-1}. **^{1}H NMR** (400 MHz, $CDCl_3$): δ 7.95 (d, $J = 8.0$ Hz, 1H Ar–H), 7.86 (d, $J = 8.0$ Hz, 1H Ar–H), 7.76 (t, $J = 8.0$ Hz, 4H Ar–H), 7.64 (d, $J = 8.0$ Hz, 1H Ar–H), 7.57 (d, $J = 8.0$ Hz, 2H Ar–H), 7.49 (t, $J = 8.0$ Hz, 1H Ar–H), 7.38 (t, $J = 8.0$ Hz, 2H Ar–H), 7.10 (t, $J = 8.0$ Hz, 1H Ar–H), 6.95 (s, 1H Ar–NH-). **^{13}C NMR** (100 MHz, $CDCl_3$): δ 147.1, 145.8, 140.9, 139.2, 137.8, 136.3, 135.0, 130.3, 130.2, 129.9, 129.1, 128.9, 126.9, 126.0, 123.3, 119.7. **HRMS (ESI):** m/z $[M + H]^+$ calcd for $C_{20}H_{15}ClN_3^{\ +}$: 332.0949; found: 332.0950. The LC–MS and NMR spectra are shown in figures S1, and S2 respectively.

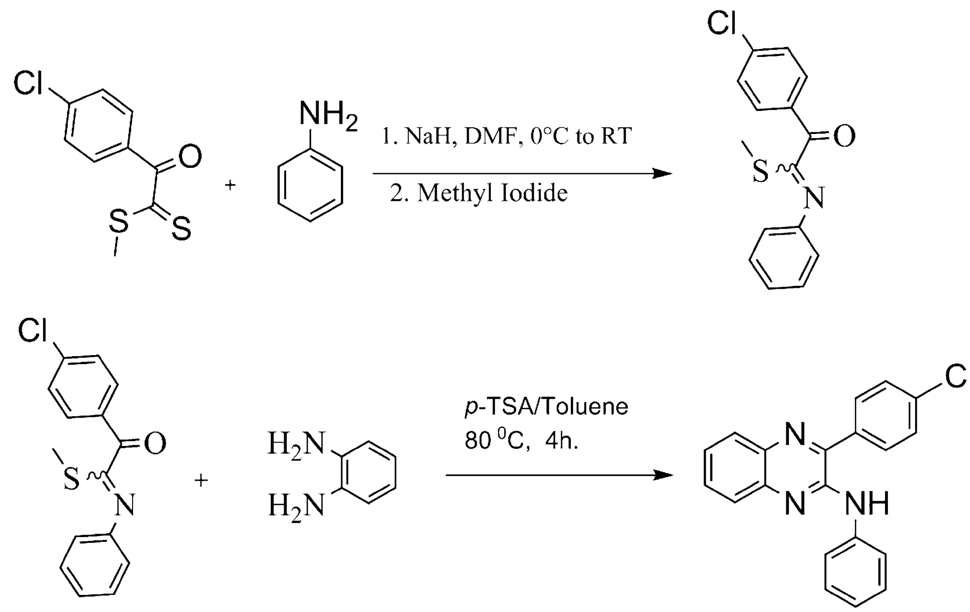

Fig. 1 Reaction pathway for the synthesis of 3-(4-chlorophenyl)-*N*-phenylquinoxalin-2-amine

Experimental details

A yellow colored rectangular shaped crystal with dimensions 0.22 × 0.21 × 0.20 mm^3 was selected for the single crystal X-ray diffraction (XRD) study. The X-ray intensity data were collected on a Bruker APEX3 D8 Venture diffractometer equipped with graphite monochromator using Mo*Kα* radiation. A complete data set was processed using *SAINT* software [23]. The structure was solved by direct methods and refined by full-matrix least-squares on F^2 using SHELXS and SHELXL programs [24] respectively. Non-hydrogen atoms were refined anisotropically. The hydrogen atoms were placed at geometrical positions and allowed to ride on their parent atoms. A total of 217 parameters were refined with 4440 unique reflections. The residual parameter converged to 0.055. The geometrical calculations were performed using *PLATON* program [25]. Oak Ridge Thermal Ellipsoid Plot (*ORTEP*) and molecular packing diagrams were generated using *Mercury* [26]. A summary of the crystal data and refinement details are listed in Table 1.

Table 1 Crystal data and structure refinement details

Empirical formula	$C_{20}H_{14}CLN_3$
Formula weight	331.79
Temperature	293(2) K
Wavelength	0.71073 Å
Crystal system	Orthorhombic
Space group	$P2_12_12_1$
Cell dimensions	a = 5.7410(14) Å, b = 8.881(2) Å, c = 31.188(8) Å
Volume	1590.2(7) $Å^{-3}$
Z	4
Density(calculated)	1.386 Mg m^{-3}
Absorption coefficient	0.245 mm^{-1}
F_{000}	688
Crystal size	0.15 mm × 0.20 mm × 0.30 mm
θ range for data collection	3.02° to 29.60°
Index ranges	$-7 \le h \le 7$ $-12 \le k \le 12$ $-43 \le l \le 43$
Reflections collected	25,872
Independent reflections	4440 [R_{int} = 0.060]
Refinement method	Full matrix least-squares on F^2
Data / restraints / parameters	4440/0/217
Goodness-of-fit on F^2	1.093
Final [$I > 2\sigma(I)$]	$R1 = 0.0550$, $wR2 = 0.1407$
R indices (all data)	$R1 = 0.0669$, $wR2 = 0.1505$
Flack parameter	0.08(3)
Largest diff. peak and hole	0.420 and − 0.310 e $Å^{-3}$

Results and Discussion

Crystal Structure Analysis

The compound $C_{20}H_{14}CLN_3$ crystallizes in the orthorhombic crystal system with the space group $P2_12_12_1$. The unit cell parameters are a = 5.7410(14) Å, b = 8.881(2) Å, c = 31.188(8) Å. The ORTEP of the molecule is shown in Fig. 2. The crystal data and refinement details are listed in Table 1.

The molecular structure consists of chlorophenyl ring, phenyl ring, and the quinoxaline ring. The bond distances and bond angles are in good agreement with the standard

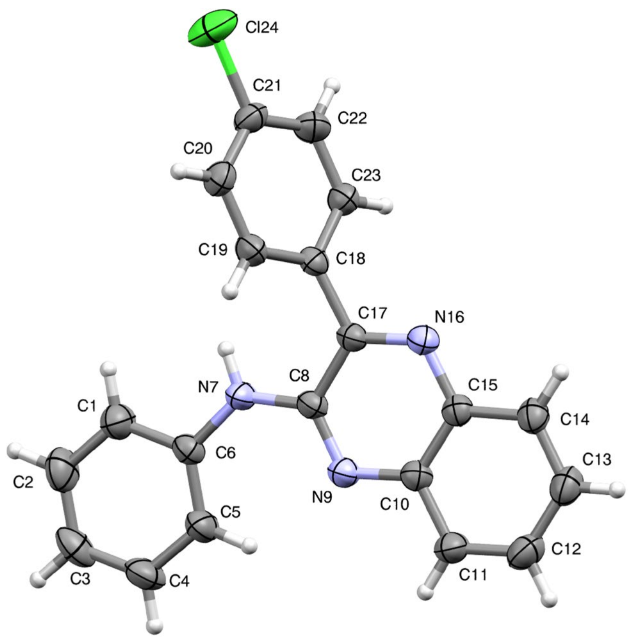

Fig. 2 ORTEP of the 3-(4-chlorophenyl)-*N*-phenylquinoxalin-2-amine drawn at 50% probability

values [27]. Selected bond lengths, bond angles, and torsion angles are listed in Tables 2, 3, and 4 respectively. The bond distance of N7–C8 (1.363(4) Å) indicates the single bond nature, while the bond distance of 1.313(4) Å for the N9–C8 atoms indicates the double bond. The atoms C2–C1–C6, C1–C2–C3, C2–C3–C4, C3–C4–C5, and C4–C5–C6 shows trigonal geometry as their bond angle avereaged to 120°. The torsion angle of N9–C10–C11–C12 atoms is 178.0(3)° which indicates the + *anti*-periplanar conformation as well as the value of − 178.5(2)° of atoms C19–C20–C21–Cl24 indicates the − *anti*-periplanar conformation. The phenyl ring C8–N9–C10–C15–N16–C17 has planar conformation with a maximum r.m.s. deviation of 0.03(3)Å for the N9

Table 2 Selected bond lengths of the molecule obtained from XRD analysis and DFT calculation

Atoms	Length (Å)		Atoms	Length (Å)	
	XRD	DFT		XRD	DFT
Cl24–C21	1.737(3)	1.756	C10–C11	1.414(4)	1.416
N7–C6	1.407(4)	1.407	C11–C12	1.372(5)	1.382
N7–C8	1.363(4)	1.377	C12–C13	1.398(5)	1.416
N9–C8	1.313(4)	1.317	C14–C15	1.405(4)	1.415
N9–C10	1.363(4)	1.364	C17–C18	1.492(4)	1.492
C1–C6	1.391(4)	1.409	C18–C19	1.396(4)	1.405
C2–C3	1.371(5)	1.398	C22–C23	1.387(4)	1.393
C4–C5	1.394(5)	1.397	C8–C17	1.453(4)	1.463

Table 3 Selected bond angles of the molecule obtained from XRD analysis and DFT calculation

Atoms	Angle (°)		Atoms	Angle (°)	
	XRD	DFT		XRD	DFT
C6–N7–C8	131.1(2)	131.6	C12–C13–C14	120.6(3)	120.1
C8–N9–C10	116.8(2)	118.0	C13–C14–C15	119.6(3)	119.8
C15–N16–C17	117.6(3)	118.8	N16–C15–C10	120.2(3)	120.1
C2–C1–C6	120.7(3)	120.7	C10–C15–C14	120.3(3)	120.0
C1–C2–C3	120.4(4)	120.3	N16–C15–C14	119.5(2)	119.7
C2–C3–C4	119.0(3)	118.9	C8–C17–C18	121.8(2)	122.7
C3–C4–C5	121.7(3)	121.4	N16–C17–C8	121.6(3)	120.5
C4–C5–C6	119.6(3)	119.4	C19–C18–C23	118.4(3)	118.5

atom. The quinoxaline ring is also planar with a maximum r.m.s. deviation of 0.038(3)Å for the C10 atom.

The phenyl rings are sp^2 hybridized. The structure exhibits C–H···π interactions and C–CL···π interaction. C3–H3···Cg4 interaction: H–Cg4 distance is 2.74 Å, C–H···Cg4 angle is 138°, C–Cg4 distance is 3.489(4) Å. The hydrogen bond interactions are listed in the Table 5. The packing of molecules when viewed down *a* axis is shown in Fig. 3. The structure is reinforced by C–H···N intramolecular interactions. The structure is further stabilized by π–π interactions. The strong π-stackings show short centroid–centroid contacts (< 3.8 Å), small slip angles (β, γ < 25°) and vertical displacements (< 1.5 Å) [28]. A few selected π-π interactions are listed in the Table 6.

Hirshfeld Surface Analysis

Hirshfeld surface analysis is a tool used to visualize intermolecular interactions. The 2D fingerprint plots summarize the nature and type of intermolecular contacts in the crystal structure qualitatively. The Hirshfeld surfaces are mapped with the d_{norm} function, where d_{norm} is the normalized contact distance which is a surface property and is given by

$$d_{\mathrm{norm}} = \frac{d_i - r_i^{vdw}}{r_i^{vdw}} + \frac{d_e - r_e^{vdw}}{r_e^{vdw}},$$

where d_i and d_e are the distances from the nearest nucleii inside and outside of the molecule from the Hirshfeld surface respectively. r_i^{vdW} and r_e^{vdW} are the van der Waals radii internal and external to the surface respectively [29].

Hirshfeld surfaces and 2D fingerprint plots were generated using *CrystalExplorer17* [30]. The Hirshfeld surface mapped over d_{norm} and corresponding/associated fingerprint plots are shown in Fig. 4. The intermolecular C–H···C interactions are indicated by red spots on the d_{norm} surface. The fingerprint plots show the various contributions to the total Hirshfeld surface area. The interactions are shown in the

Table 4 Selected torsion angles of the compound obtained from XRD analysis and DFT calculation

Atoms	Angle (°)		Atoms	Angle (°)	
	XRD	DFT		XRD	DFT
C6–N7–C8–N9	2.8(5)	− 1.84	N9–C10–C15–N16	4.1(4)	− 3.2
C8–N7–C6–C1	176.1(3)	173.2	N9–C10–C15–C14	− 177.5(3)	178.1
C6–N7–C8–C17	− 178.2(3)	179.8	N9–C10–C11–C12	178.0(3)	− 178.3
C8–N9–C10–C11	177.5(3)	− 179.7	C10–C11–C12–C13	0.2(5)	− 0.05
C17–N16–C15–C14	− 178.6(3)	179.3	C12–C13–C14–C15	− 0.5(5)	0.13
C2–C1–C6–N7	− 178.5(3)	178.7	C19–C18–C23–C22	1.0(4)	0.99
C2–C1–C6–C5	0.7(5)	− 0.2	C18–C19–C20–C21	1.7(4)	− 0.33
C2–C3–C4–C5	0.6(6)	0.03	C19–C20–C21–Cl24	− 178.5(2)	− 179.5

Table 5 Hydrogen bond geometry parameters (Å)

D–H···A	D–H (Å)	H···A (Å)	D···A (Å)	D–H···A (°)
C5–H5···N9*	0.93	2.30	2.909(4)	123

*Intramolecular interaction

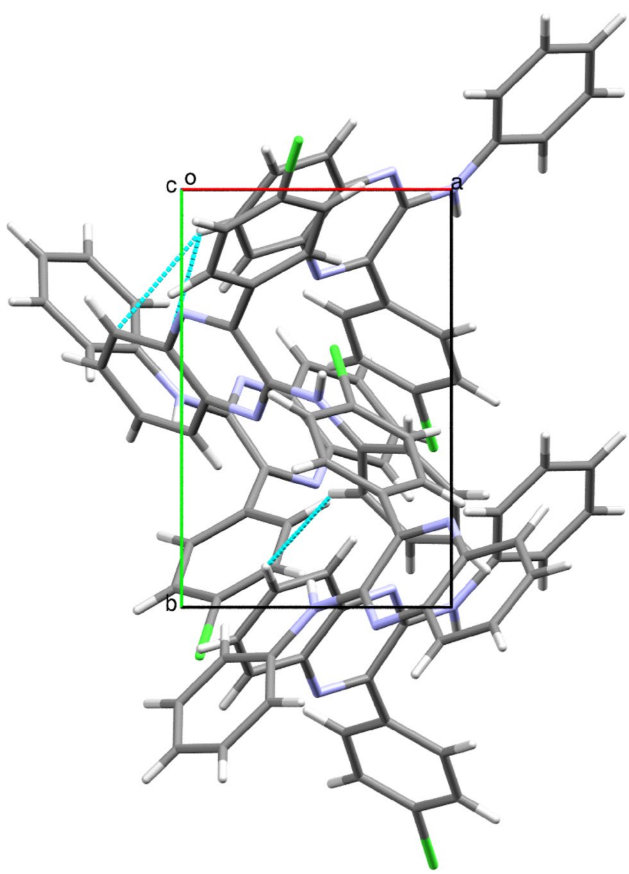

Fig. 3 Packing of molecules when viewed along *c* axis

decomposed fingerprint plots, which are considered as the feature of short, significant contacts [31]. The different contacts are listed in Table 7. The highest contribution is from H···H contacts and least contribution is from N···H contacts.

Energy Frameworks

The energy frameworks provide way to envisage the interaction energy between the molecular pairs in the crystal structures. The energy frameworks is computed by *CrystalExplorer17* software [30]. The molecular pairs are constructed around the center of molecule within a distance of 3.8 Å. It gives the information about the type of energies responsible for the supramolecular assembly of crystal packing in the molecular system [32].

According to Mackenzie et al., the benchmarked energies used to construct the energy framework in the calculation are scaled [33]. The cylinders indicate the relative strengths of molecular packing in energy frameworks in different directions. The absence of the cylinders in a direction attributed to the weak interactions. The interactions between the molecular pairs are dispersion (193.5 kJ/mol), electrostatic (− 36.6 kJ/mol), polarization (− 7.5 kJ/mol), and repulsion (119.2 kJ/mol) energies. The energy interactions show the predominance of the dispersion energy over the electrostatic energy. Molecular packings corresponding to electrostatic energy (red), dispersion energy (green), and total energy (blue) along *a, b*, and *c* axis respectively are shown in Fig. 5. Different interaction energies are listed in Table 8.

Density Functional Theory

Density Functional Theory is a theoretical method to study the electronic and structure properties of the molecule. The structural parameters of the compound are geometrically optimized by DFT calculations using *Gaussian09* software [34] with B3LYP hybrid functional [35] and 6–31 + G(d, p) basis set in the gaseous phase. The bond distance of N–C atoms is similar to the calculated bond distance of N–C atoms (Tables 2, 3, and 4). Theoretically calculated

Table 6 Selected Cg-Cg interactions involved in the molecule

CgI	CgJ	CgI–CgJ	α (°)	β (°)	γ (°)	CgI_perp (Å)	CgJ_perp (Å)	Slippage (Å)
Cg1	Cg2[a]	3.564(2)	0.36(15)	14.6	14.8	−3.4451(11)	−3.4482(14)	0.900
Cg2	Cg5[b]	3.6634(19)	1.63(13)	19.3	18.6	−3.4725(14)	−3.4577(9)	1.210

a = 1 + *x, y, z*

b = -1 + x, y, z

structural parameters are in good agreement with the XRD values. The slight deviations in theoretical values are due to the fact that XRD calculations were done in gaseous phase. The reults are affirmed by the correlation coefficients between the experimental and the theoretical values (Fig. 6). The graph shows the better agreement with the bond lengths and bond angles with the correlation coefficient $R^2 = 0.991$ and $R^2 = 0.933$ respectively.

Frontier Molecular Orbitals

The highest occupied molecular orbital (HOMO) and lowest unoccupied molecular orbital (LUMO) are used to analyse the charge transfer interactions taking place within the molecule. The energy levels of HOMO and LUMO for the molecule were computed using DFT via B3LYP method with the 6–31 G (d, p) basis set using *Gaussian09* software [34]. Figure 7 depicts the energy levels of frontier molecular orbitals. The HOMO as an electron donor represents the ability to donate an electron; LUMO represents the ability to accept an electron. The energy gap between the HOMO and LUMO is an important parameter in determining the molecular electron transport properties and the chemical reactivity of the molecule. HOMO–LUMO energy gap explains the charge transfer interactions taking place within the molecule.

The energies of HOMO (E_{HOMO}), E_{LUMO}, energy gap and other molecular descriptors such as ionization potential (I), electron affinity (A), electronegativity (χ), global hardness (η), and global softness (σ) are listed in Table 9. According to by Koopmann's theorem, the energy of HOMO is correlated to the ionization potential (IP) and the LUMO energy is used to calculate the electron affinity (EA). The average value of energies of HOMO and LUMO is related to the electronegativity (χ), as $\chi = (IP + EA)/2$. The term electrophilicity index (ω) is defined as $\omega = \mu^2/2\eta$ where μ is the chemical potential taking the average value $\mu = -(IP + EA)/2$. Domingo et al. [36] established an electrophilicity (ω) scale for the classification of organic molecules as strong electrophiles with $\omega > 1.5$ eV, moderate electrophiles with $0.8 < \omega < 1.5$ eV, and marginal electrophiles with $\omega < 0.8$ eV. The gap between HOMO–LUMO is the excitation energy of electrons from ground state. In terms of chemical reactivity, soft molecules are more rective than the hard molecules due to their smaller HOMO–LUMO gaps [37]. The energy gap of title compound (3.61 eV) indicates that it is a soft molecule.

Topology Analysis

Quantum theory of atoms in molecules (QTAIM) provides insights into the intramolecular interactions present in the molecule. Th presence of intramolecular interaction helps to stabilize the crystal structure in molecular systems [38]. Quantum theory of Atom in molecule (AIM) analysis shows the presence of C–H···N intramolecular interaction, which is also observed in the experimental XRD analysis (Table 5). The C5–H5···N9 intramolecular interaction confirmed by both experimental and theoretical studies. Figure 8 displays the atoms showing C–H···N intramolecular interaction. Further, N–H···C intramolecular interaction is also observed.

QTAIM analysis describes the different types of bonding interactions using electron density ($\rho(r)$), potential energy (V(r)), Laplacian of electron density ($\nabla^2\rho$), and Lagrangian kinetic energy (G(r)). If the values of $\nabla^2\rho(r) > 0$ and ratio of $-G(r)/V(r) > 1$, then the interactions are non-covalent. Table 10 lists the topology parameters and hydrogen bond interactions present in the molecule. It shows that the interactions are non-covalent in nature as their ρ(r) values are less than 0.10 a.u and laplacian values are all positive and lie within the range 0.124 to 0.182. The values of $-G(r)/V(r)$ for the interactions are greater than unity, which is an indication of a non-covalent interactions and also the ratio of $|\lambda_1|/\lambda_3$ must be less than one for non-covalent interactions [39].

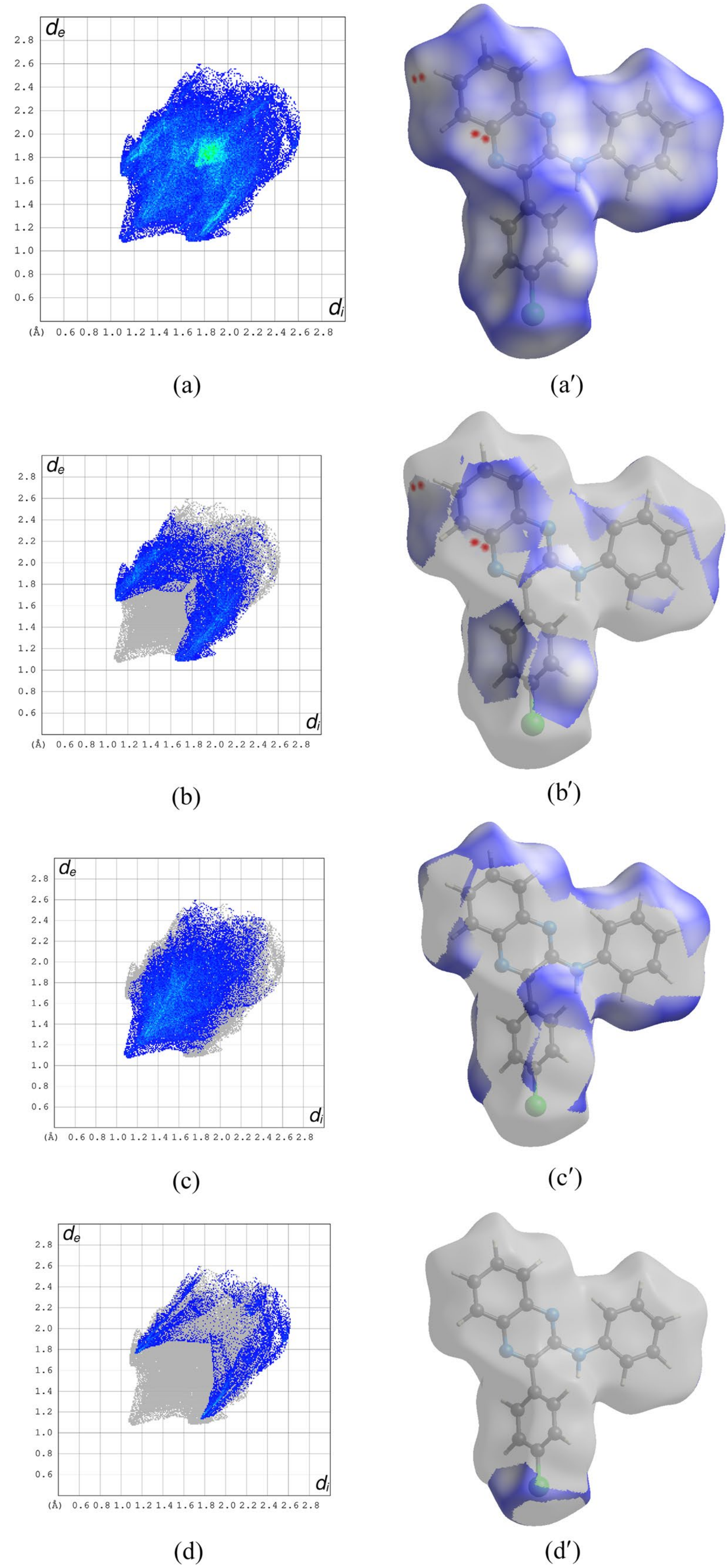

Fig. 4 Fingerprint plots of individual contacts associated with Hirshfeld surfaces indicating. **a** H–H contacts, **b** C–H/H–C contacts, **c** N–H/H–N contacts, and **d** CL–H/H–CL contacts respectively

Table 7 Individual contributions to the Hirshfeld surface area

Intercontacs	Contributions (%)
H–H	43.2
C–H/H–C	25.6
CL–H/H–CL	10.8
N–H/H–N	7.2

The presence of weak and medium hydrogen bonds in the molecule was analysed by the interaction energy. The interaction energy of C5–H5···N9 is − 13.123 kJ/mol shows the strong hydrogen bond interaction and N–H···C interaction shows − 9.350 kJ/mol.

Molecular Electrostatic Potential

Molecular electrostatic potential (MEP) surface is used to analyse the electrophilic and nucleophlic sites present in a molecule. The electrostatic potential is represented by different color schemes. The red colored and blue colored regions on the molecular electrostatic potential map indicate the strong electrophilic and nucleophilic sites in the molecule respectively. MEP is defined as $V(r) = Z_A/(R_A - r)$, where $V(r)$ is the potential energy at r, Z_A is the charge on the nucleus [40]. The molecular electrostatic potential map is generated using *Gaussian09* software [34] with the B3LYP/6–31 G(d, p) basis set. The MEP map indicating the electrophilic and nucleophilic sites is shown in Fig. 9. Figure 9 shows the electrophilic sites

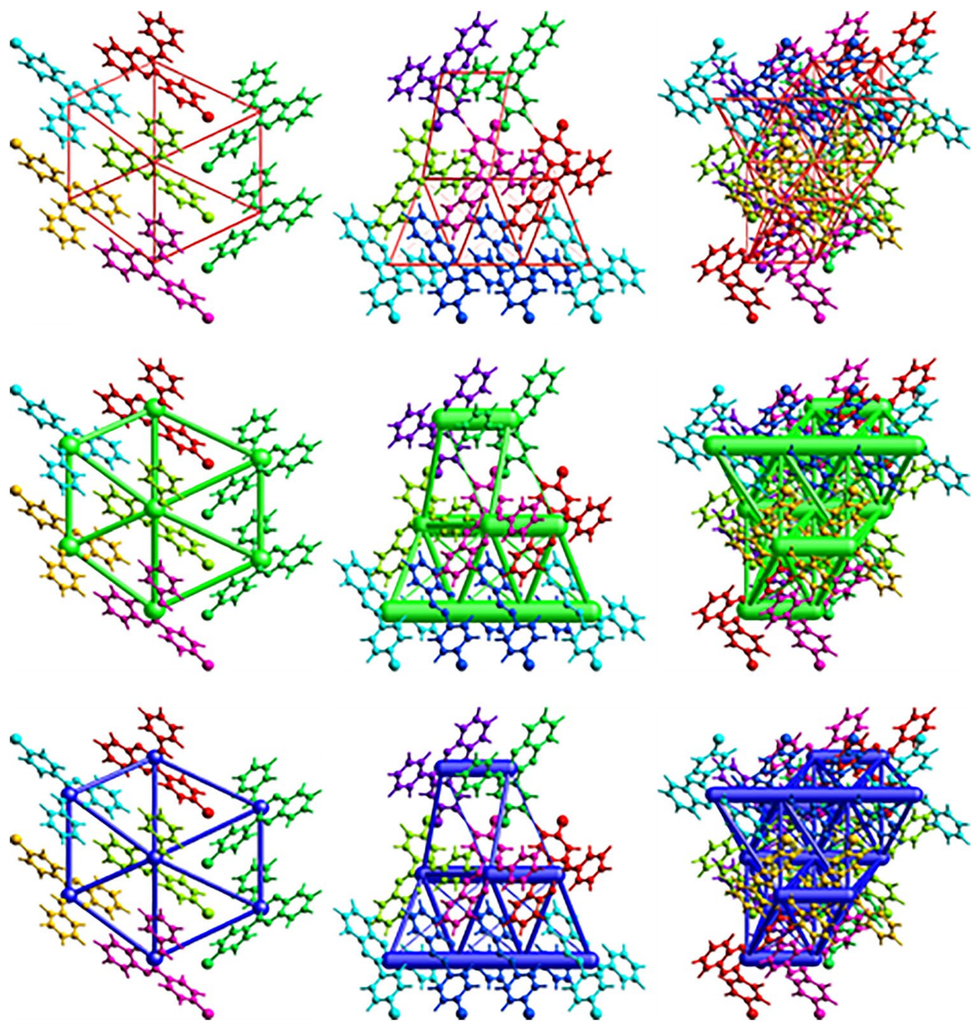

Fig. 5 Molecular packing corresponding to electrostatic energy, dispersion energy, and total energy along *a, b*, and *c* axis respectively

Table 8 Interaction energies

	N	Symop	R	E_ele (kJ/mol)	E_pol (kJ/mol)	E_dis (kJ/mol)	E_rep (kJ/mol)	E_tot (kJ/mol)
	2	x, y, z	10.58	-5.2	-0.6	-22.8	16.0	-16.0
	2	x+1/2, -y+1/2, -z	8.52	-5.3	-0.6	-22.3	13.8	-16.9
	2	x, y, z	5.74	-7.7	-3.5	-74.3	40.6	-50.3
	2	-x, y+1/2, -z+1/2	9.24	-6.3	-1.0	-22.5	18.8	-15.3
	2	x+1/2, -y+1/2, -z	13.30	-0.8	-0.2	-7.5	3.8	-5.1
	2	x+1/2, -y+1/2, -z	10.54	-5.9	-0.4	-21.5	15.7	-15.6
	2	-x, y+1/2, -z+1/2	9.88	-1.6	-0.2	-5.8	2.2	-5.6
	2	x, y, z	8.88	-3.8	-1.0	-16.8	8.3	-14.2

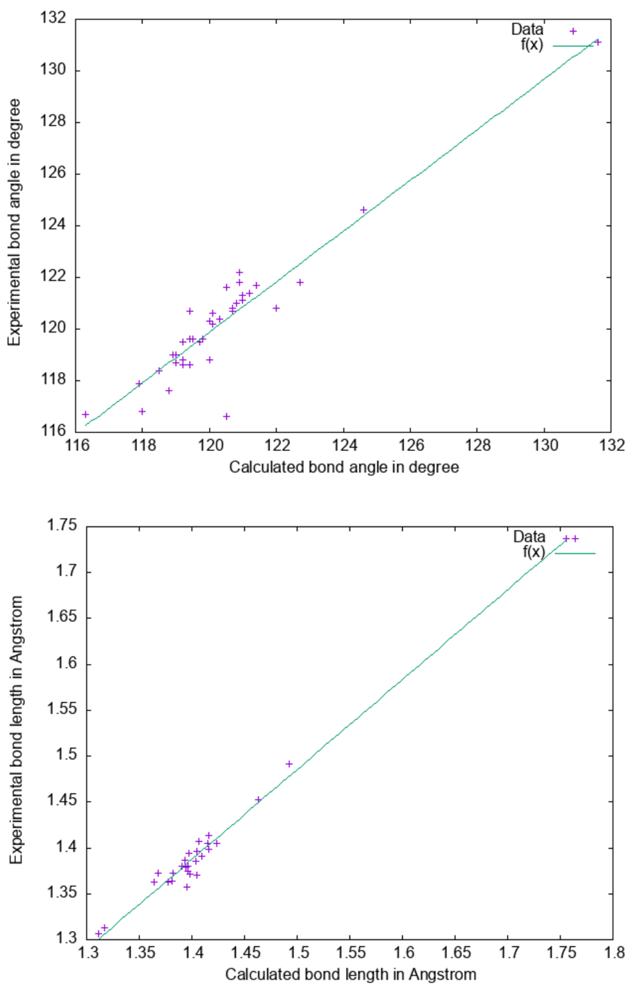

Fig. 6 Correlation graph between the calculated and experimental bond distances, and bond angles

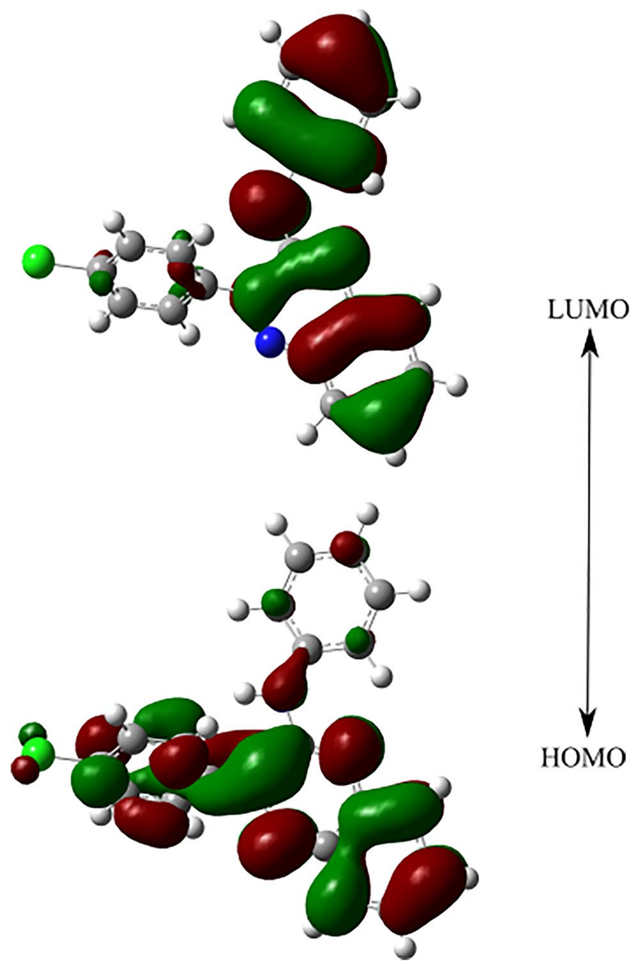

Fig. 7 HOMO and LUMO of the molecule

Table 9 Molecular descriptor and their energies

Descriptor	Energy
E_{HOMO}	− 5.79 eV
E_{LUMO}	− 2.18 eV
Energy gap (ΔE)	3.61 eV
Ionization potential (IP)	5.79 eV
Electron affinity (EA)	2.18 eV
Chemical potential (μ)	− 3.98 eV
Electronegativity (χ)	3.98 eV
chemical hardness (η)	1.81 eV
Global softness (σ)	0.55 eV^{-1}
Electrophilicity (ω)	4.39 eV

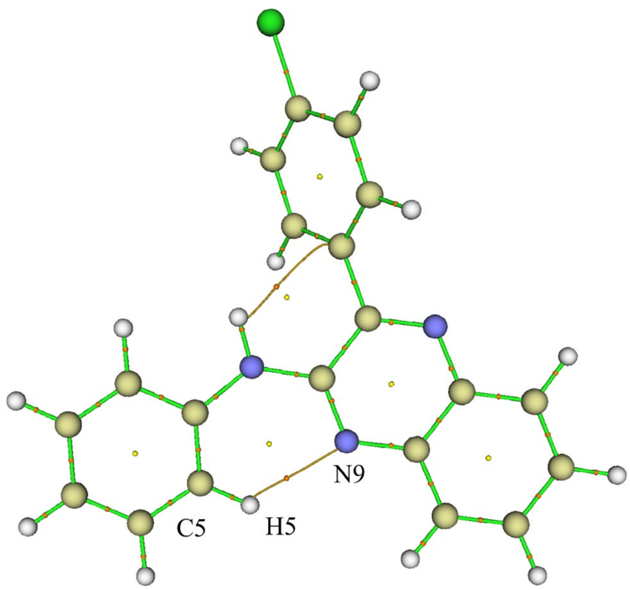

Fig. 8 Atoms showing C–H⋯N intramolecular interaction

(blue) are around the nitrogen atom of quinoxaline ring while nucleophilic region (red) is around the hydrogen atom. The presence of electronegative nitrogen atom in the compound will enhances the structural stability and bioactivity within the molecule [41].

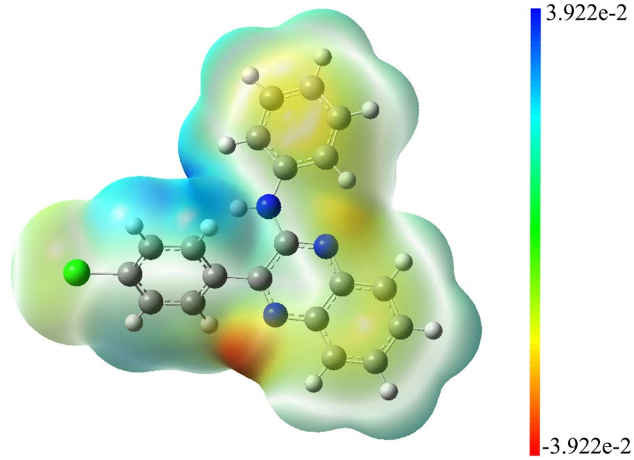

Fig. 9 Molecular electrostatic potential map of the molecule

Reduced Density Gradient (RDG)

Reduced density gradient R(*r*) is a topological method employed to visualize the non-covalent interactions (NCIs) like hydrogen bond interactions, van der Waals interactions and steric effects in the molecule. It is a function of electron density $\rho(r)$ and its gradient. The equation for (R(*r*)) is given by

$$R(r) = \frac{1}{2\left(3\pi^2\right)^{1/3}} \frac{|\nabla \rho(r)|}{\rho(r)^{4/3}}.$$

RDG is a dimensionless quantity [42]. DFT calculations were performed using *Gaussian09* [34] software with B3LYP/6–31 G(d, p) basis set. The RDG plot was generated by *Multiwfn* [43] and *VMD* [44] software. The RDG was analysed by plotting R(*r*) against the product of the density and the sign of the second eigenvalue of electron density of Hessian matrix (sign(λ_2) ρ(*r*)). The 2D scatter plot and corresponding RDG isosurface of the molecule is shown in Fig. 10.

The sign of λ_2 was used to distinguish between the regions of strong attraction ($\lambda_2 < 0$) and strong repulsion ($\lambda_2 > 0$).

Table 10 Topological parameters (a.u.) and hydrogen bond energies (kJ/mol) obtained by QTAIM analysis

Interaction	ρ(*r*)	$\nabla^2\rho$	*V*(r)	*G*(r)	$\frac{-G(r)}{V(r)}$	λ_1	λ_2	λ_3	$\frac{\lvert\lambda_1\rvert}{\lambda_3}$	E_{HB}
C5–H5⋯N9	0.017394	0.05841	− 0.011438	0.013021	1.13822	− 0.0175	− 0.01643	0.0923579	0.18957	− 13.123
N7–H7⋯C18	0.013350	0.05248	− 0.00829	0.010706	1.291336	− 0.010325	− 0.00248	0.0652984	0.158129	− 9.350

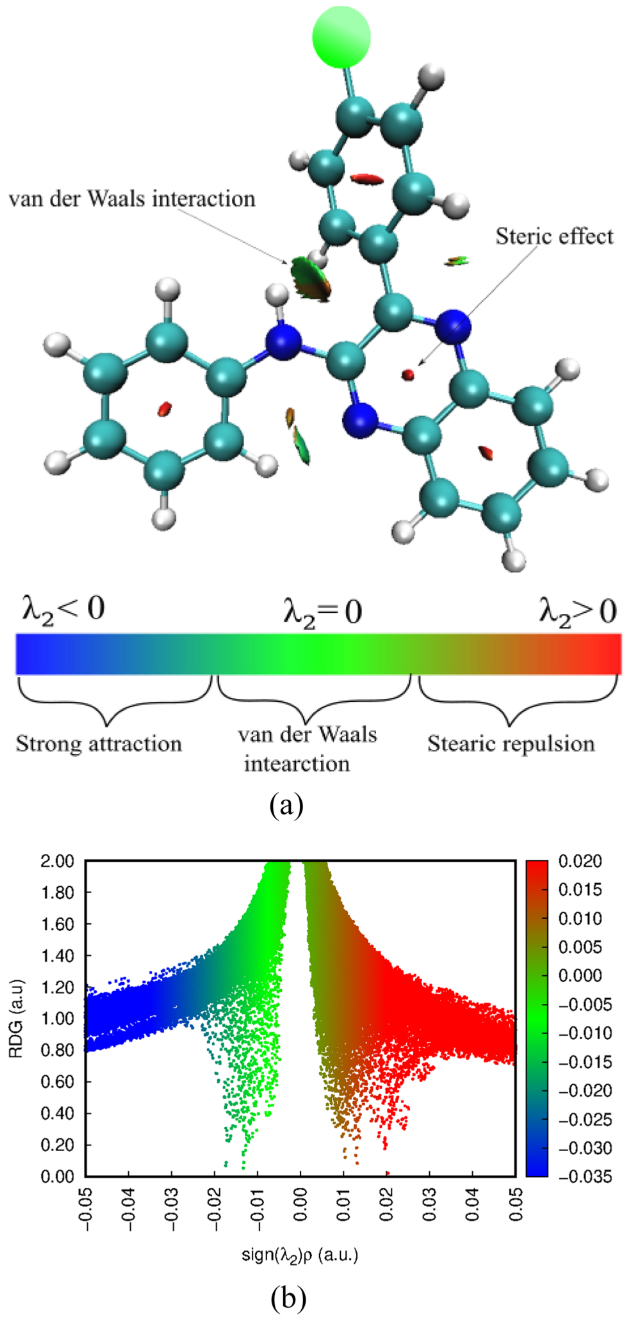

Fig. 10 The RDG isosurface (a) and 2D scattered plot (b) of the molecule

Figure 10a shows the van der Waals interactions between H atom of the phenyl and N8 atom of the quinoxaline ring. Steric repulsion was observed at the canter of the quinoxaline ring, chlorophenyl ring and a benzene ring. A strong hydrogen bond is absent in the compound. The right peak (Fig. 10b) with red color corresponds to steric repulsion (center of the quinoxaline ring) with the sign(λ_2) ρ(r) value in the range 0.01–0.02 a. u. van der Waals interactions and steric clashes are represented with the isosurface value of 0.6.

Conclusions

The molecule crystallizes in the orthorhombic crystal system with the space group $P2_12_12_1$. Hirshfeld surface studies confirm the presence of C–H···N intramolecular interaction in the molecule. The fingerprints plot show that the highest contribution to the overall Hirshfeld surface area is from H–H (43.2%) contacts. Comparison of experimental and theoretical bond lengths and bond angles shows good agreement. The energy difference between the HOMO and LUMO is 3.61 eV. The MEP analysis indicates that the reactive sites of the molecule are around nitrogen and hydrogen atoms around the rings.

Supplementary Information The online version contains supplementary material available at https://doi.org/10.1007/s10870-022-00959-9.

Acknowledgements Akhileshwari P. thanks to DST-KSTePS, Government of Karnataka, Bengaluru. Thanks to SAIF, IIT Madras, Chennai.

Author Contribution All authors have contributed in preparation of the manuscript. PA: Conceptualization and Interpretation of the data, visualization, methodology, and writing-original draft of the manuscript. KRK: Synthesis and spectroscopic characterization. MAS: Investigation, supervision, and approval of the final version of the manuscript.

Declarations

Conflict of interest The authors declare no conflict of interest.

References

1. Al-Marhabi RA, Abbas HS, Ammar YA (2015) Molecules 20:19805–19822. https://doi.org/10.3390/molecules201119655
2. Ahmed EA, Mohamed MFA, Omran A, Salah H (2020). Synth Commun. https://doi.org/10.1080/00397911.2020.1787448
3. Ismail MMF, Amin KM, Noaman E, Soliman DH, Ammar YA (2010) Eur J Med Chem 45:2733–2738
4. Yoo HW, Lee YS, Suh ME, Kim DJ, Park SW (1998) Arch Pharm 10:331–333
5. Pereira JA, Pessoa AM, Cordeiro MNDS, Fernandes R, Prudencio C, Noronha JP, Vieira M (2015) Eur J Med Chem 97:664–672
6. El Newahie A, Nissan Y, Ismail N, El Ella AD, Khojah S, Abouzid K (2019) Molecules 24(6):1175. https://doi.org/10.3390/molecules24061175
7. Alswah M, Ghiaty A, El-Morsy A (2013) K El-Gamal 587054:1–7. https://doi.org/10.1155/2013/587054
8. Saadaoui I, Krichen F, Salah BB, Mansour R, Miled N, Bougatef A, Kossentini M (2018). J Mol Str. https://doi.org/10.1016/j.molstruc.2018.12.008
9. El-Zahabi SAH (2017) Arch. Pharm. Chem. Life Sci. 350:e1700028. https://doi.org/10.1002/ardp.201700028
10. Fabian L, Porro MT, Gómez N, Salvatori M, Turk G, Estrin D, Moglioni A (2020) Eur J Med Chem 188(111987):0223–5234. https://doi.org/10.1016/j.ejmech.2019.111987
11 Elzupir AO, Ali MKM, Hussein RAH, Ibrahem MA, Al-Muhanna MK, Ibnaouf KH (2018). J Mol Str. https://doi.org/10.1016/j.molstruc.2018.10.035

12. Montana M, Montero V, Khoumeri O, Vanelle P (2020) Molecules 25:2784. https://doi.org/10.3390/molecules25122784
13. Oyallon B, Botineau BM, Logé C, Robert T, Bach S, Ibrahim S, Raoul W, Croix C, Berthelot P, Guillon J, Pinaud N, Gouilleux F, Massuard MV, Sabourin CD (2021) Molecules 26:867. https://doi.org/10.3390/molecules26040867
14. Karzazi Y, Belghiti ME, El-Hajjaji F, Hammouti B (2016) J Mater Environ Sci 7(10):3916–3929
15. Kumar A, Kumar S, Saxena A, De A, Mozumdar S (2008) Catal Commun 9:778–784
16. Raja B, Balachandran V, Revathi B, Anitha K (2018). Mater Res Innov. https://doi.org/10.1080/14328917.2018.1477544
17. Dahbi S, Methnani E, Bisseret P (2010) Tetrahedron Lett 51:5516–5520
18. Asif M (2016) Euro Rev Chem Res 8:31–51
19. Arthur F, Michael L, Graham S (2012) J Org Chem 45:1909–1919
20. Richard JK (2003) Chem Commun 18:2286–2287
21. Lainne SE, Suling WJ, Reynolds RC (2002) J Med Chem 45(25):5604–5606
22. Kiran KR, Swaroop TR, Santhosh C, Rangappa KS, Sadashiva MP (2021) ChemistrySelect 6:1–5. https://doi.org/10.1002/slct.202102071
23. Bruker (2012) SAINT PLUS. Bruker AXS Inc., Madison, Wisconsin
24. Sheldrick GM (2008) Acta Cryst Sec A 64:112–122
25. Spek AL (1990) Acta Cryst Sec A 46:34
26. Macrae CF, Bruno IJ, Chisholm JA, Edgington PR, McCabe PE, Pidcock E, Rodriguez-Monge L, Taylor R, van de Streek J, Wood PA (2008) J App Cryst 41:466–470
27. Allen FH, Kennard O, Watson DG, Brammer L, Orpen AG, Taylor RJ (1987) Chem Soc Perkin Trans 2(12):S1–S19
28. Yang XJ, Drepper F, Wu B, Sun WH, Haehnel W, Janiak C (2005) Dalton Trans 2:256–267. https://doi.org/10.1039/B414999H
29. Spackman MA, Jayatilaka D (2009) Cryst Eng Commun 11:19–32
30. Turner MJ, McKinnon JJ, Wolff SK, Grimwood DJ, Spackman PR, Jayatilaka D, Spackman MA (2017) *CrystalExplorer17.5*
31. Spackman MA, McKinnon JJ (2002) Cryst Eng Comm 4(66):378–392. https://doi.org/10.1039/B203191B
32. Mackenzie CF, Spackman PR, Jayatilaka D, Spackman MA (2017) IUCrJ 4:575–587
33. Turner MJ, Thomas SP, Shi MW, Jayatilaka D, Spackman MA (2015) Chem Commun 51:3735–3738
34. Gaussian 09, Revision A.02, Frisch MJ, Trucks GW, Schlegel HB, Scuseria GE, Robb MA, Cheeseman JR, Scalmani G, Barone V, Petersson GA, Nakatsuji H, Li X, Caricato M, Marenich A, Bloino J, Janesko BG, Gomperts R, Mennucci B, Hratchian HP, Ortiz JV, Izmaylov AF, Sonnenberg JL, Williams-Young D, Ding F, Lipparini F, Egidi F, Goings J, Peng B, Petrone A, Henderson T, Ranasinghe D, Zakrzewski VG, Gao J, Rega N, Zheng G, Liang W, Hada M, Ehara M, Toyota K, Fukuda R, Hasegawa J, Ishida M, Nakajima T, Honda Y, Kitao O, Nakai H, Vreven T, Throssell K, Montgomery Jr JA, Peralta JE, Ogliaro F, Bearpark M, Heyd JJ, Brothers E, Kudin KN, Staroverov VN, Keith T, Kobayashi R, Normand J, Raghavachari K, Rendell A, Burant JC, Iyengar SS, Tomasi J, Cossi M, Millam JM, Klene M, Adamo C, Cammi R, Ochterski JW, Martin RL, Morokuma K, Farkas O, Foresman JB, Fox DJ (2016) Gaussian, Inc., Wallingford CT. https://gaussian.com
35. Tirado RJ, Jorgensen WL (2008) J Chem Theory Comput 4(2):297–306. https://doi.org/10.1021/ct700248k
36. Domingo LR, Aurell MJ, Pérez P, Contreras R (2002) Tetrahedron 58(22):4417–4423. https://doi.org/10.1016/S0040-4020(02)00410-6
37. Pearson RG (2005) J Chem Sci 117(5):369–377
38 Kumar PSV, Raghavendra V, Subramanian V (2016) J Chem Sci 128(10):1527–1536
39. Lohith TN, Hema MK, Karthik CS, Sandeep S, Mallesha L, Alsaiari NS, Sridhar MA, Katubi KM, Abualnaja KM, Lokanath NK, Mallu P (2022) J Mol Stru 26:133378. https://doi.org/10.1016/j.molstruc.2022.133378
40. Jayappa M, Akhileshwari P, Sridhar MA, Nagarajappa L, Nagaraju S, Raghavendra S, Jayappa M (2021) Eur J Chem 12(1):69–76. https://doi.org/10.5155/eurjchem.12.1.69-76.2067
41. Eimre K, Urgel JI, Hayashi H, Giovannantonio MD, Ruffieux P, Sato S, Otomo S, Chan YS, Aratani N, Passerone D, Groning O, Yamada H, Fasel R, Pignedoi CA (2022) Nat Commun 13:511. https://doi.org/10.1038/s41467-022-27961-1
42 Laplaza R, Peccati FA, Boto R, Quan C, Carbone A, Piquemal J, Maday Y, Garcia JC (2020) J WIREs Comput Mol Sci 1497:1–18. https://doi.org/10.1002/wcms.1497
43. Lu T, Chen F (2012) J Comput Chem 33:580–592. https://doi.org/10.1002/jcc.22885
44. Humphrey W, Dalke A, Schulten KJ (1996) J Mol Graph 14(1):33–38. https://doi.org/10.1016/0263-7855(96)00018-5